JOURNAL OF AIRCRAFT
Vol. 37, No. 2, March–April 2000

Acoustics and Unsteady Flow of Telescope Cavity in an Airplane

G. R. Srinivasan*
NASA Ames Research Center, Moffett Field, California 94035-1000

The Stratospheric Observatory for Infrared Astronomy consists of a 2.5-m aperture Cassegrain telescope housed in an open cavity onboard a Boeing 747-SP aircraft cruising at around 13 km altitude. The open cavity of this airborne observatory presents many aerodynamic and aeroacoustic challenges that are being resolved for its design using results from computational and experimental investigations. Results are reported from one such Navier–Stokes computational fluid dyanamics (CFD) investigation on an overset grid system at wind-tunnel and cruise flight conditions. Numerical results of sound pressure levels, spectra of unsteady pressures on the telescope and bulkheads, spectra of telescope moments, and time-averaged surface pressures on the empennage show fair comparisons with experiments. An acoustic tone at 440 Hz has been identified for this cavity from CFD calculations at wind-tunnel conditions, and this acoustic tone is in agreement with experimental observation. The good agreement of scaled wind-tunnel results with computational results at cruise conditions indicates the scaling relations used are accurate. The open cavity produces a drag increase of less than 2% of the aircraft drag and is found to have negligible effect on the aircraft controls in cruise flight.

Nomenclature

A	= telescope axial force
a_∞	= freestream sound speed
C_p	= pressure coefficient, $(p - p_\infty)/q_\infty$
Dt	= nondimensional time step, dta_∞ / l
dt	= physical time step
f_m	= Rossiter frequency
h_c	= cavity depth
k_v	= constant, see Eq. (2)
L	= length of aircraft
l	= characteristic length scale
l_c	= cavity aperture length in x direction
M	= Mach number
N	= telescope normal force
PM, RM, YM	= telescope moments (pitch, roll, and yaw), see Fig. 10
p	= fluid pressure
p_∞	= freestream static pressure
q_∞	= freestream dynamic pressure, $0.5\rho_\infty U_\infty^2$
Re	= Reynolds number
S	= wing planform area
SF	= telescope side force
Sr	= Strouhal number, $f_m(l_c/U_\infty)$
U_∞	= freestream velocity
x, y, z, t	= physical space coordinates
x_T, y_T, z_T	= telescope based coordinate system, see Fig. 10
α	= angle of attack, deg
α_c	= constant, see Eq. (2)
γ	= ratio of specific heats for air
δ	= boundary-layer thickness
ρ	= fluid density

Subscripts

c	= cavity
T	= telescope
∞	= freestream

Presented as Paper 98-0413 at the AIAA 36th Aerospace Sciences Meeting, Reno, NV, 12–15 January 1998; received 22 February 1998; revision received 6 October 1999; accepted for publication 8 October 1999.

*Chief Scientist, Raytheon Systems Company. Associate Fellow AIAA.

Introduction

THE Stratospheric Observatory for Infrared Astronomy (SOFIA) consists of a 2.5-m aperture Cassegrain telescope with a Nasmyth focus and is housed in an open cavity in the Boeing 747-SP aircraft. This airborne observatory will fly in the Earth's stratosphere between altitudes of 12.5 and 14.1 km for infrared viewing of celestial objects in the universe. At this altitude, in the clear, dry environment on the edge of space, SOFIA will enable researchers to study radiant heat patterns from stars, planets, and other celestial sources. SOFIA is a follow-on mission to the NASA's Kuiper Airborne Observatory (KAO) that was decommissioned in 1995. When it becomes operational, SOFIA will possess capabilities significantly greater than the KAO and offer advantages over other Earth- and space-based instruments. SOFIA is a joint program between NASA and the German Aerospace Research Center, DLR. Figure 1 shows SOFIA in flight.

In the last few years many experimental[1–3] and computational investigations[4–12] have been performed to understand and resolve design problems associated with the open cavity environment of the SOFIA. These issues include reducing shear-layer oscillations and accompanied cavity noise, reducing dynamic loads on the telescope for providing better pointing accuracy, minimizing the drag increase of the open cavity to maximize time of the mission, and, finally, reducing the impact of the open telescope bay on the control surfaces for preserving the stability of the aircraft.

There have been many experimental and computational investigations in the literature on the cavity flow problem.[13–30] Many of the fluid flow and acoustic issues of these investigations are similar to the present problem. The results of these studies, however, are not directly useful to the present configuration. Even the large body of experimental data available from the earlier developmental research on KAO[29,30] is not directly useful to the SOFIA developmental program because of differences in aircraft platform, cavity location, aperture size and shape, telescope configuration, and cruise flight conditions.

The SOFIA design has thus far progressed utilizing results from both wind-tunnel experiments and computational fluid dynamics (CFD) simulations on a 7% scale model. Different aircraft platforms (Boeing 747-SP and 747-200), cavity aperture shapes, telescopes, and many shear-layer control devices have been considered in these investigations. Just like in KAO development, the cavity location started out on the forward section of the fuselage behind the cockpit, but was later moved to a more favorable downstream location behind the wings with the aperture on the port side of the aircraft. Both forward and aft located cavity configurations were the subject of the first Navier–Stokes investigations by Atwood[4,6,7] and

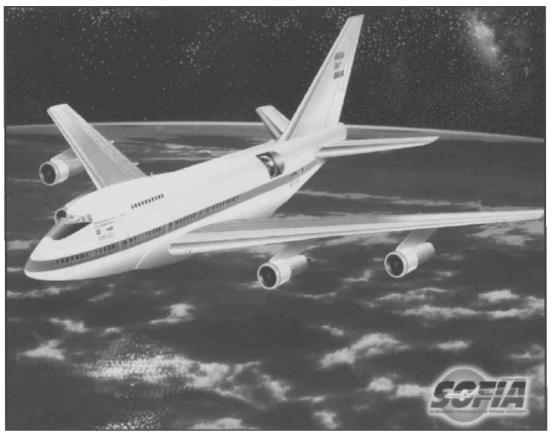

Fig. 1 SOFIA in cruise flight.

Atwood and Van Dalsem.[5] The CFD geometry used in these investigations was a sting-mounted 7% wind-tunnel (WT) scale model of the Boeing 747-SP aircraft without empennage. The cavity had a circular aperture with a tub-type telescope mounted in it. Subsequent computational investigations by Klotz[8] and Srinivasan[9,10] used similar scale models of the Boeing 747-SP and 747-200 aircraft, respectively, but included a complete empennage. Some of the results from these earlier investigations are presented elsewhere.[10–12]

The results from CFD simulations not only complement the experimental database, but will also provide detailed flowfield information that is difficult to measure in a WT test. The present CFD investigation is one such study designed to evaluate the influence of cavity aperture and telescope shape on cavity acoustics and unsteady flow in the cavity and on the aircraft at WT and cruise flight conditions. In particular, the suitability of a D-shaped cavity aperture, a split (fixed and moveable) aft ramp at the downstream end of the cavity aperture for shear-layer control, and a truss telescope are evaluated using the Boeing 747-SP aircraft platform by comparing CFD results of cavity acoustics and unsteady flow with experimental data. Comparison of CFD results at flight conditions with experimental data and CFD results at WT conditions will determine the suitability of the scaling laws currently being used.

Numerical Procedure

The numerical method solves the Reynolds-averaged Navier–Stokes equations on an overset grid framework using the flow solver OVERFLOW.[31] This flow solver uses a central-difference, implicit, diagonal algorithm[32] with added second- and fourth-order numerical dissipation. The numerical scheme is second-order accurate in space and first-order accurate in time. For turbulent viscous flows, the nondimensional viscosity coefficient μ is computed as a sum of $\mu_l + \mu_t$, where the laminar viscosity μ_l is determined using Sutherland's law and the turbulent viscosity μ_t is calculated using the Baldwin–Lomax algebraic eddy viscosity model.[33] In the present computations the boundary layer in the cavity and on the entire aircraft is assumed to be fully turbulent. The eddy viscosity in the shear layer over the cavity is computed as outlined by Buning[31] using a shear-layer model.

The boundary conditions are applied explicitly in the computations. A no-slip boundary condition is specified at the wall with zero normal pressure gradient along with an adiabatic wall condition. Characteristic boundary conditions are specified at the far-field boundary. To update the information exchange at the overset grid interface, a trilinear interpolation of the dependent variables is used. The computations have been performed on the Numerical Aerodynamic Simulation (NAS) and Aeronautics Consolidated Supercomputer Facility (ACSF) Cray C-90 supercomputers at the NASA Ames Research Center. The flow solver cost is 6.7 μs/iteration/grid point on these supercomputers for the algorithm options described.

The grid generation process involves two steps. First, the surface grid definitions are downloaded from CAD definitions and converted into NASA initial graphics exchange specification (IGES) format. This information is then used in the GRIDGEN code,[34] an interactive surface grid generation program, to construct surface grids. Second, volume grids containing O–O, C–O, and H–H topology are generated from the surface descriptions using HYPGEN code,[35] a hyperbolic grid generator. For the 7% WT model of the Boeing 747-SP aircraft, all 22 aircraft grids were ported from earlier investigations.[5,8] The 19 cavity grids were generated by Klotz.[36] Figure 2 shows a view of surface grids and sample volume grids for the wing, horizontal tail, and fuselage. The truss telescope geometry was simplified in the CFD model by neglecting cross members connecting the telescope base (containing primary and tertiary mirrors) to the truss yoke and truss spyderyoke. The secondary mirror, connected to the spyderyoke by cross-member elements, was also neglected. Thus, a three-part truss telescope grid was constructed using the aforementioned grid generation tools. Figure 3 shows a view of the cavity surface grids and the truss telescope base. As shown, the cavity is isolated from the pressurized aircraft main cabin by the forward and aft bulkheads. The CFD geometry of the aircraft with cavity and telescope assembly has a total of 44 overset grids containing about 5.3×10^6 grid points for the entire flowfield domain. The grid clustering near the wall and the spacing of the first grid point

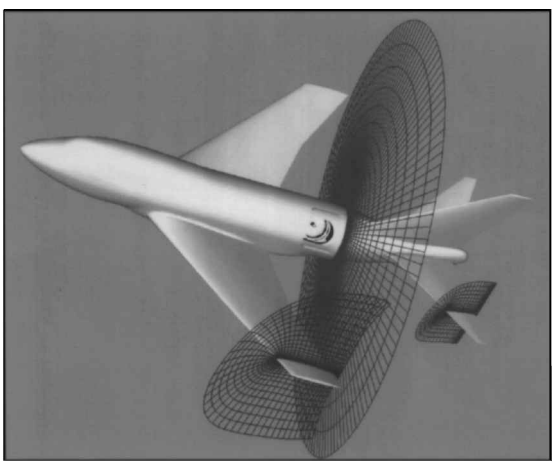

Fig. 2 View of the surface and volume grids used in the SOFIA geometry.

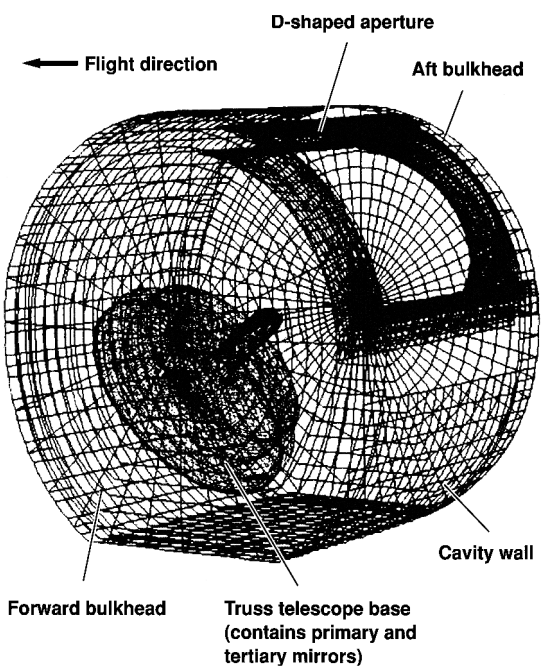

Fig. 3 Surface grids of cavity walls and telescope base containing primary and tertiary mirrors.

from the solid surface is important for resolving the boundary layer. In the present grids, the spacing of the first grid point is different for each grid and varies in the range from $2 \times 10^{-5} l$ to $5 \times 10^{-5} l$, where l is the characteristic length of each grid surface. This spacing of first grid point from the surface translates to y^+ values of between 1.0 and 2.2 in different grids.

The intergrid boundaries of the Chimera overset grids are generated by running the PEGSUS code.[37,38] Creating proper hole shape and interface boundaries is an iterative process and requires several attempts of hole cutting and (surface and volume) grid generation until all grid points in the computational domain are properly interpolated. Although tedious, the Chimera hole cutting is a necessary step in the overall solution process of this complex geometry containing many overset grids.

Discussion of Results

Numerical results of unsteady flow and acoustics are presented for a 7% WT scale model at WT and flight conditions of a freestream Mach number of $M_\infty = 0.85$ and aircraft angle of attack $\alpha = 2.5$ deg. The corresponding Reynolds numbers are, respectively, $Re = 13.1 \times 10^6$/m and 72.8×10^6/m. The CFD geometry of the aircraft and cavity was exactly reproduced from the WT scale model but the telescope was simplified. The CFD calculations used free-air boundaries and did not model WT walls.

In the present configuration of SOFIA, the D-shaped cavity aperture is located 5.08 cm inside the fuselage moldline. The cavity length in the flow direction is $l_c = 18.9$ cm, and its depth is $h_c = 15.75$ cm. The cavity, thus, has a length to depth ratio of $l_c / h_c = 1.2$ measured at its aperture and is nearly 0.9 measured from the fuselage moldline. The aperture has a split (fixed and moveable) ramp at the downstream end of the cavity for shear-layer control. A barrel door will enable the cavity aperture to be completely closed during takeoff and landing of the aircraft. Located inside the cavity is a truss telescope. The telescope base houses the primary and tertiary mirrors. The cavity and the telescope assembly contains 22 overset grids consisting of 3.2×10^6 grid points; the aircraft platform has 22 grids consisting of an additional 2.1×10^6 grid points.

In the calculation procedure, a pseudosteady solution is generated first and the unsteady calculation is initiated from this. The unsteady solution is advanced in a time-accurate fashion using a constant, nondimensional time step of $Dt = 0.12$. This time step translates to a dimensional $dt = 9\ \mu$s of real WT time and 128 μs in cruise flight. This value of dt used in the computations is the stability-limited time step size of the numerical code. The cavity grids, including the shear-layer grid, used a much smaller time step of $dt/3$. This reduced time step corresponds to a Courant–Friedrichs–Lewy (CFL) number of about 1 in the streamwise direction within the shear layer and a $\mathrm{CFL}_{\max} \simeq 500$. Unsteady flowfield solution and telescope loads data were collected for a total duration of 0.16 and 2.37 s real time, respectively, in WT and cruise flight CFD simulations. This time corresponds to advancing the unsteady solution by 18,500 time steps with constant dt. By comparison, a typical continuous data trace of a WT experiment, to which the CFD results are compared, is approximately 5 s long. Computationally, each CFD solution required about 300 Cray C-90 h, including the initial pseudosteady calculation.

Time-averaged surface pressure coefficients C_p were calculated for the vertical and horizontal tails from the unsteady flowfield data. Figure 4 shows a comparison of CFD results with experimental data for the vertical tail at two representative cross sections JJ and KK. The agreement of the two results is good, even though the total duration of the CFD unsteady data is only $\frac{1}{30}$th of the experimental data trace. The C_p along the midchord of the port and starboard sides of the vertical tail show some discrepancy with experiments in the tail root region ($z/L \leq 0.15$) and around the maximum thickness point. A similar discrepancy was also observed in previous computations for the vertical tail.[10] Inspection of flow on the vertical tail indicated the flow to be completely attached for most parts except in the trailing-edge region on the port side of tail root where the flow appears very unsteady. Figure 5 presents similar time-averaged surface

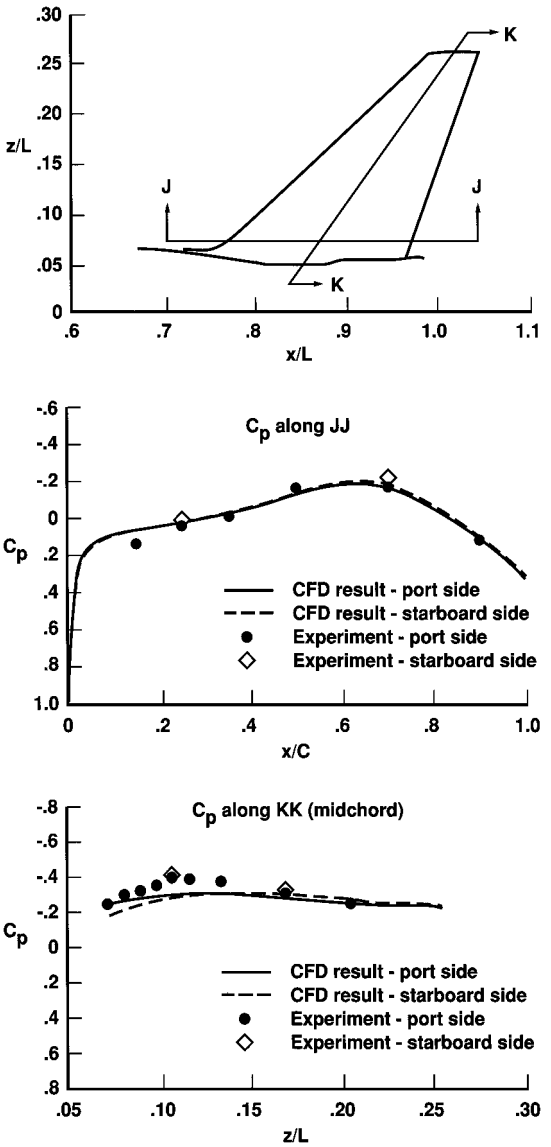

Fig. 4 Comparison of computed and experimental time-averaged surface pressure coefficients on vertical tail at WT condition of $M_\infty = 0.85$, $\alpha = 2.5$ deg, and $Re = 13.1 \times 10^6$/m.

pressure comparisons for the port side horizontal tail along its leading edge and midchord. The CFD results show a good agreement with experiments for the leading edge. The C_p distribution along the midchord shows good agreement with experiments for the lower surface and a fair agreement for the upper surface. Comparison of CFD C_p distributions for the port and starboard sides of the horizontal tail show very small differences in the two distributions. The comparison of C_p distributions and the comparison of surface particle traces (not shown here) indicate that the open cavity does not have any major impact on the empennage flow, and, in particular, the effectiveness of control surfaces and the stability of the aircraft are essentially undisturbed.

The flowfield near the cavity and its immediate vicinity shows that these regions are tremendously influenced by the open cavity environment.[39,40] Figure 6 shows the instantaneous surface particle flow visualizations in these regions viewed by two different methods. Figure 6a shows a plot of velocity vectors on a plane one grid point above the solid surface. This plot, similar to an experimental tufts survey, clearly identifies regions of flow separation and flow singularities in the aperture area within the recessed hole and on the aft ramp part of the cavity aperture. These topological features of the flow are more clearly identified in the surface particle flow picture of Fig. 6b. The view clearly identifies the existence of three

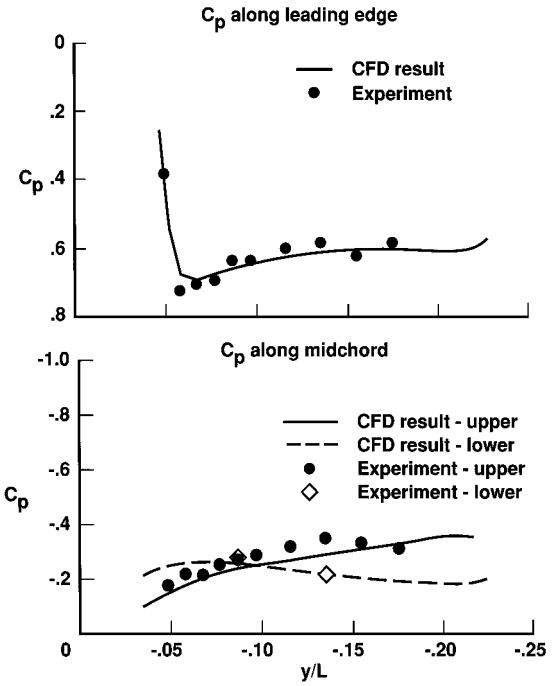

Fig. 5 Comparison of computed and experimental time-averaged surface pressure coefficients on horizontal tail at WT condition.

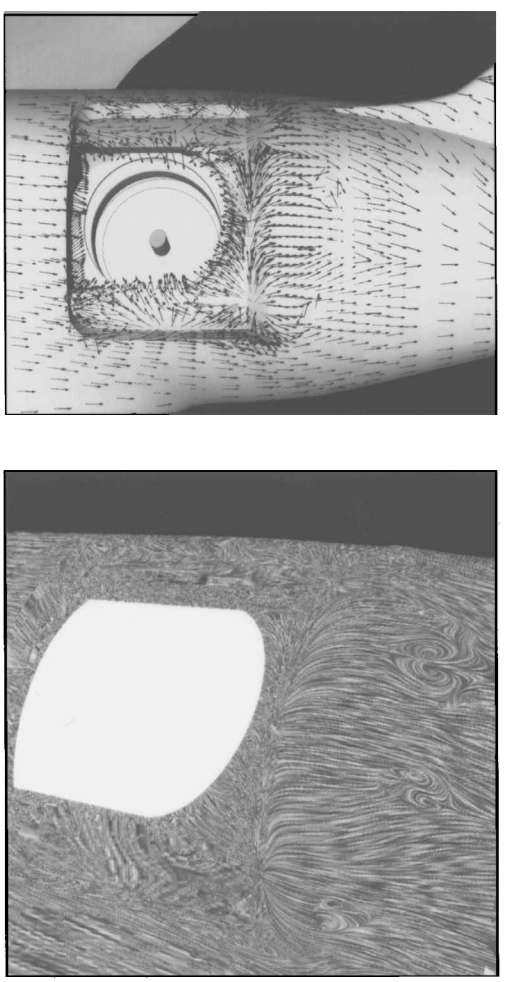

Fig. 6 Views of computed a) surface velocity vectors and b) surface particle flow in the vicinity of cavity aperture and aft ramp region at one grid point away from the surface at WT condition.

counter-rotating vortical flow structures in the aft ramp region of the cavity aperture.

The surface particle flow of Fig. 6b is a textured map[41] created using the line integral convolution algorithm[42] by releasing massless particles at a given instant from several locations on a plane of a grid one grid point away from the surface and then following the particle paths determined by the unsteady velocity field. Such data sets released at a series of consecutive time steps are used to create streak lines. This postprocessor software toolkit has been used successfully before to explain the physics of separation and vortex breakdown on an oscillating delta wing.[43] As seen, the present recessed D-shaped cavity is apparently producing a more complex separated flow pattern compared to the circular aperture cavity of the previous investigations.[8–12] The large extent of flow separation seen on the moveable part of the aft ramp of the present aperture configuration appears to recover quickly by reattaching downstream on the fixed part of the aft ramp. This reattachment of the flow is also reflected in the behavior of surface pressure that becomes uniform downstream of the ramp.

One of the important parameters contributing to the problem of cavity resonance is the nature and thickness of the boundary layer immediately upstream of it. To understand if the present CFD grids are resolving the boundary layer on the aircraft adequately, separate steady calculations were run on a 7% scale model of the Boeing 747-200 aircraft platform. Both WT and flight test data are available for this platform (as the Space Shuttle carrier) to compare with CFD results. The flight test data were measured at a slightly lower freestream Mach number ($M_\infty = 0.6$) than the present cruise flight Mach number ($M_\infty = 0.85$). To compensate for the lower freestream Mach number the data were measured at a lower altitude (10.7 km) than the present cruise altitude (13.1 km) where CFD simulations are run. Note that the forward sections of the Boeing 747-SP and 747-200 aircraft fuselages are nearly identical and that the 747-200 aircraft has a stretched fuselage. The small differences in the empennage geometries are assumed to be unimportant from the point of boundary-layer growth on the fuselage. Both 747-SP and 747-200 aircraft CFD models used grids similar in dimension and clustering at the body surface. Comparisons of CFD and experimental boundary-layer profiles and boundary-layer growth at WT and flight conditions show reasonably good agreement with each other, as shown in Fig. 7. This suggests adequate resolution and clustering of CFD grids at the surface.

A list of sound pressure levels (SPL) determined from CFD and experiment at the locations of experimental pressure tranceducers on the telescope primary mirror and bulkheads is presented in Table 1. The physical intensity of an acoustic wave is measured on a decibel scale by the SPL as follows:

$$\mathrm{SPL} = 20 \log_{10}(p_{\mathrm{rms}} / p_{\mathrm{ref}}) \tag{1}$$

where p_{rms} is the root mean square of the fluctuating pressure and p_{ref} is the reference pressure that corresponds to the weakest audible sound (or threshold of hearing at 1 kHz) for an average person. A value of $p_{\mathrm{ref}} = 2 \times 10^{-5}$ N/m^2 is assumed in this study.

Experimental results of SPL are determined from 5-s-long pressure–time traces, whereas the CFD SPL are determined from pressure–time traces that are substantially brief, namely, 0.16 s for the WT simulation and 2.3 s for the cruise flight simulation. In contrast to the nearly continuous sampling of experimental data, the CFD data is saved at every 25 time steps in the WT simulation runs and at every 5 time steps in the flight simulation runs. The flight simulation data have, therefore, five times the sampling data points available for determining SPL and spectra compared to WT simulation data.

The SPL calculated at F1 on the forward bulkhead from both WT and flight CFD results has a fair comparison to the experimentally determined value. Likewise, the CFD result of SPL at location A1 on aft bulkhead also has a fair comparison with experimental value, but the CFD result at A2 shows a 5.5-dB higher value than the experimental value. Because SPL has been calculated from CFD solutions at all surface grid points on the bulkheads, inspection of these results reveals the location A2 on the aft bulkhead and its immediate

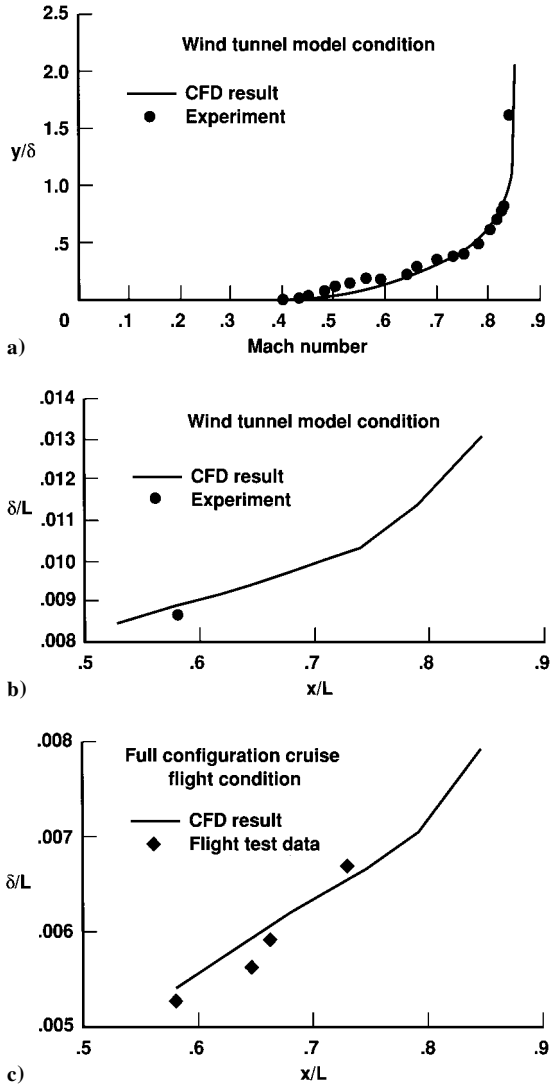

Fig. 7 Computed and measured a) boundary-layer profile at x/L = 0.58 and boundary-layer thickness along the SOFIA platform (Boeing 747-200 aircraft), b) at WT, and c) at flight conditions.

surroundings to have higher SPL values of 1–6 dB compared to the rest of the aft bulkhead surface. Visualization of Mach number and pressure contours from the CFD solution in this region shows the existence of highly unsteady flow accompanied by high-pressure zones. These regions are also found to be associated with higher fluctuating pressures due to the flow ingestion into the cavity from the bull-nose region of the aperture. In contrast, the forward bulkhead shows relatively uniform pressure and has no high-pressure regions on its surface.

The SPL determined for the locations on upper and lower surface of the telescope primary mirror show the scaled flight CFD results to WT conditions to be in general agreement with experimentally determined values. The differences seen between the two are of the same order as the uncertainties found in the experimental data. In contrast, the SPL determined from the CFD WT simulation run are consistently higher than the experimental values, perhaps due to fewer sampling points available from the shorter data trace for this simulation. Simple numerical experiments done to calculate SPL have shown that errors of the order of 2–4 dB are introduced in SPL due to the brevity of the unsteady data trace and the smaller number of sampling points used in determining SPL. The discrepancy in results determined from the CFD solutions with experiments may have also occurred because of 1) the use of a simplified geometry for the telescope, 2) the treatment of WT walls as free-air boundaries in CFD simulation, and 3) how often the unsteady data are collected during the computational simulation.

Table 1 Computed and experimental SPL on the telescope and bulkheads at pressure tap locations (T = top and B = bottom) shown

Location	WT CFD result, dB	Flight CFD result scaled to WT condition, dB	Experiment, dB
T1	141.3	137.7	138.5
T2	140.7	136.1	136.1
T3	142.1	136.8	136.7
T4	139.4	138.2	136.4
T5	142.0	138.9	136.8
T6	137.9	139.5	137.3
T7	142.4	138.4	137.0
T8	140.3	134.9	138.3
B1	140.0	138.1	137.1
B2	139.4	139.6	137.9
B3	137.9	138.8	136.2
B4	140.3	138.9	136.1
B5	140.1	140.3	136.3
B6	140.7	139.9	136.0
B7	139.3	139.2	136.4
B8	140.2	140.9	136.2
A1	138.5	136.2	135.8
A2	142.5	142.1	136.8
F1	136.9	137.3	137.8

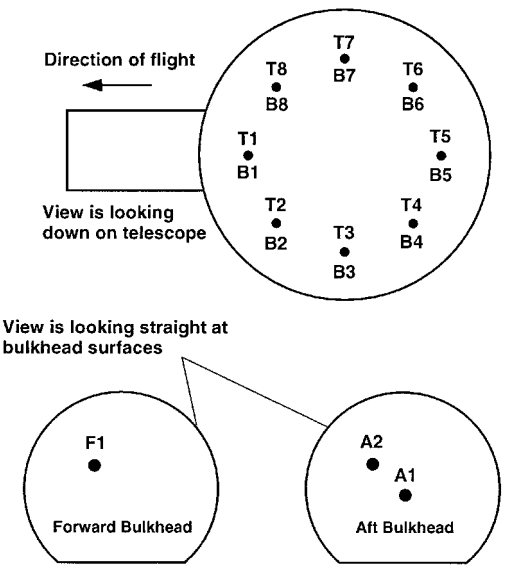

Supporting illustration to Table 1.

Spectra of SPL from unsteady surface pressures have been calculated at selected locations for the empennage, the telescope, cavity aperture, and bulkheads. The spectra for the WT CFD calculation are computed from a record containing 740 data points and zero padded to 1024 points. The flight calculation has a longer record consisting of 3700 data points and zero padded to 4096 points. The Welch windowing function[44] has been used in computing the spectra. For consistency, both experimental and CFD data were analyzed using the same spectral algorithm and windowing function. The spectra calculated for the locations F1 and A1 on the forward and aft bulkheads are presented in Fig. 8 along with experimental spectra. The flight CFD results shown have been scaled to WT conditions. Comparison of CFD and experimental spectra show the CFD result to be in fair agreement with experimental spectra only in the frequency range of 100–1500 Hz. The CFD spectra are poorly resolved in the low-frequency range mainly due to the brevity of the unsteady CFD data traces. However, at frequencies beyond 1500 Hz, the spectra show a rapid falloff due to artificial dissipation inherent in the CFD solution method. Note, however, that the contribution of acoustic energy at these higher frequencies amounts to a very small fraction of the total acoustic energy.

Figure 9 shows spectra of SPL at two pressure port locations T5 and B5 on the telescope primary mirror. The location T5 is vertically above the location B5, which is on the lower side of the

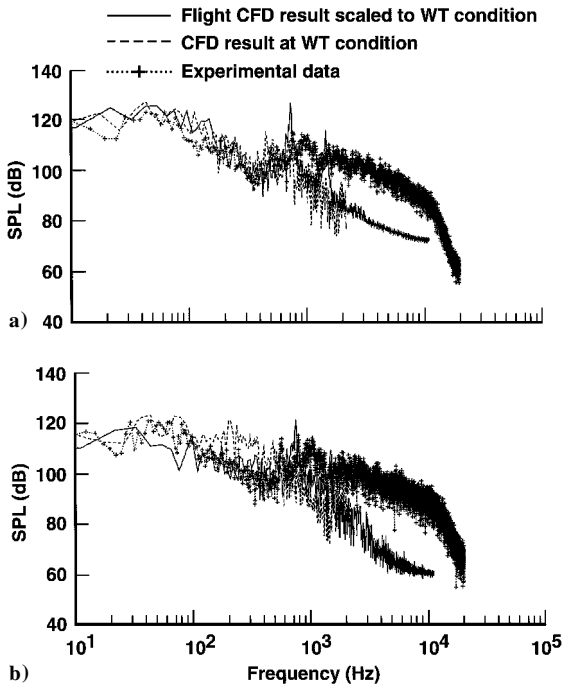

Fig. 8 Comparison of computed and experimental spectra of SPL at a) F1 on the forward bulkhead and b) A1 on the aft bulkhead at WT condition.

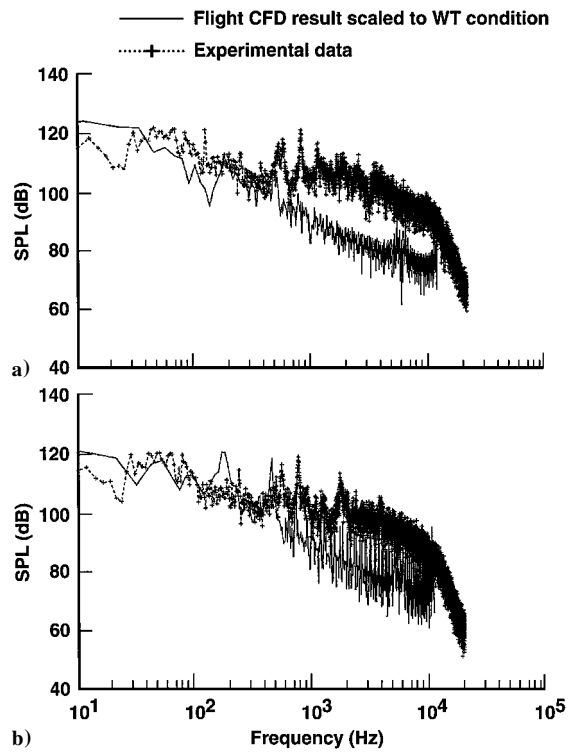

Fig. 9 Comparison of computed and experimental spectra of SPL at a) T5 on top and b) B5 on bottom of the telescope primary mirror at WT condition.

telescope primary mirror. The spectra of SPLs determined from the flight CFD results and scaled to WT conditions are presented and compared to the experimental spectra. From the sound pressure levels presented in Table 1, the CFD value of SPL at the location B5 is about 1.5 dB higher than at T5, but both locations show higher values of SPL than the corresponding experimental values. The SPL at T5 is only 0.5 dB higher than at B5 in the experiments. Simplification of the telescope geometry in the CFD model by the omission of the telescope base plate may have contributed to a higher noise level of the spectral record at B5 in the CFD result of Fig. 9, and this has resulted in producing a 4-dB higher SPL for this location. Unlike the spectra on bulkheads shown in Fig. 8, the CFD spectra on the telescope base show a fair agreement to the experimental spectra only in the frequency range of 200–1200 Hz. The level of CFD spectra is lower than experimental spectra and also appears to fall off rapidly with an increase in frequency as before; however, its frequency content seems to match with the experimental spectra to about 1200 Hz. For the reasons cited before, the CFD spectra have poor resolution at lower and higher frequencies. From the spectra presented in Figs. 8 and 9, two distinct frequencies of 440 and 730 Hz stand out to characterize the noise sources for this aperture and cavity configuration. The experimental data also show the existence of noise sources at these same frequencies. These acoustic tones correspond to 26 and 43 Hz, respectively, for the full configuration cruise flight.

The generally accepted method for predicting the frequencies of dominant acoustic modes in a cavity makes use of the Rossiter formula.[20] This formula, modified by Heller et al.,[21] is given by

$$f_m = \frac{U_\infty}{l_c}\left[\frac{m - \alpha_c}{M_\infty\sqrt{1 + [(\gamma - 1)/2]M_\infty^2} + 1/k_v}\right] \tag{2}$$

where f_m is the frequency of a given lengthwise acoustic mode, l_c is the cavity length in the streamwise direction, m is the longitudinal mode number, and γ is the ratio of specific heats for air. The constants in Eq. (2), α_c and k_v, have been determined from experimental data correlation for cavities by Rossiter.[20] The constant α_c is a function of the ratio of cavity length to its depth and is related to the phase between instabilities in the shear layer and the upstream traveling pressure waves; k_v depends on the freestream Mach number and denotes the vortex convection speed as a fraction of the freestream velocity. The particular values of these constants chosen in this study are $\alpha_c = 0.25$ and $k_v = 0.57$ following Heller et al.[21] Using the values of $U_\infty = 250.81$ m/s, $l_c = 2.7$ m, and $M_\infty = 0.85$ for the present cruise flight calculation and with the quoted empirical constants, the modified Rossiter frequency equation reduces to

$$f_m = 34.873(m - 0.25) \tag{3}$$

The frequencies determined from Eq. (3) for cruise flight condition for the first three acoustic modes corresponding to $m = 1$, 2, and 3 are 26.1, 61.0, and 95.9 Hz, respectively. The corresponding frequencies at WT conditions are 444.6, 1037.5, and 1630.3 Hz. The frequency predicted by this formula for the first acoustic tone at 444 Hz is in agreement with the WT CFD and experimental results. The corresponding Strouhal number for this first mode is 0.281.

Inspection of flow within the cavity reveals the flow to be highly unsteady and of very low speed. The flow Mach number is in the range $M \leq 0.1$ in most of the cavity. There are, however, several spots of high-pressure regions in the vicinity of the aft bulkhead and primary mirror surfaces. Visualization of particle streaks in the cavity, generated using a software toolkit called UFAT,[45] shows a strong circulatory flow in the cavity.[40] The sequence of unsteady events shows the fluid to be entering the cavity near the forward bulkhead and in the region of the aft ramp bull nose. This fluid gets mixed into the circulatory flow in the cavity. The general circulatory pattern is that the fluid particles appear to be moving away from the aft bulkhead area toward the forward bulkhead passing through the truss telescope. In the process, many of these fluid particles appear to group together to form clusters of vortical elements. These clusters of vortical fluid elements rise toward the cavity aperture and mix with the shear-layer fluid as the pressure inside the cavity increases. As the pressure in the cavity continues to increase, some of this rotating fluid exits from the cavity, and the rest of the fluid ingests into the cavity. This pattern of events of unsteady mass ingestion into the cavity and its subsequent expulsion out of the cavity repeats. The exchange of fluid from the shear layer outside the cavity with the fluid within the cavity is accompanied by periodic shear-layer impingement on the downstream ramp. This sequence of events is

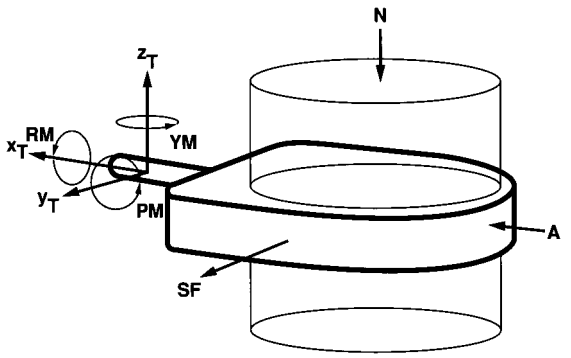

Fig. 10 Telescope coordinate system fixed to the reference frame that moves with the telescope as it rotates.

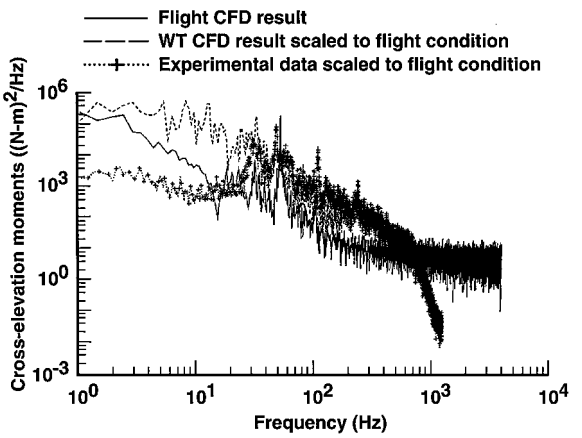

Fig. 11 Comparison of computed and experimental spectra of telescope cross-elevation moments at cruise flight condition: $M_\infty = 0.85$, $\alpha = 2.5$ deg, and $Re = 72.8 \times 10^6$/m.

clearly apparent from visualization of a movie of particle streaks entering and leaving the cavity.

The unsteady flow in the cavity will produce fluctuating airloads on the telescope and, thus, disturb its pointing accuracy. Therefore, it is important to predict dynamic loads encountered in-flight by the telescope for a proper design of its torque motors. The unsteady forces and moments are first calculated with respect to the aircraft coordinates in the present CFD procedure and then recalculated with respect to the telescope coordinate system shown in Fig. 10. The orientation of forces and moments rotate with the telescope, in the telescope coordinates (x_T, y_T, z_T), as the telescope elevation angle is changed. Figure 11 presents the spectra of telescope cross-elevation moments from the CFD calculations and experiment. Here, the CFD results, WT conditions, and the experimental data have been scaled to the full configuration flight condition. Unlike the spectra of SPL shown in Figs. 8 and 9, the spectra of telescope moments shown here are calculated from a data set containing five times more sampling points than that used in the spectra of Figs. 8 and 9. The unsteady loads calculated during the CFD solution procedure were stored at every time step of the CFD run and, therefore, contain 18,500 data points available in the unsteady data trace. This number is then zero padded to 32,768 data points for calculating the spectra of dynamic loads. As seen, these spectra are better resolved in both low- and high-frequency ranges compared to the spectra presented in Figs. 8 and 9. However, the problem appears to persist, namely, the low- and high-frequency contents of the spectra are not resolved satisfactorily for the same reasons described earlier. Over the frequency range where the spectra determined from CFD and experiment match, both CFD and experimental spectra show three distinct frequencies at 26, 43, and 103 Hz that match well with each other even though there are differences in the levels of spectra. These acoustic tones that characterize the cavity are in agreement with the dominant frequencies characterized earlier for this cavity from the spectra of SPL presented for the bulkheads and telescope.

Determination of both drag of the aircraft and drag increase due to the open cavity is one of the key objectives of the present CFD investigation. Accurate determination of the drag force from CFD, in general, is subjected to many uncertainties such as grid density, accuracy of Chimera hole boundary information, geometric complexity of the configuration under study, and the accuracy of the flow solver. Computational tools necessary to determine accurately the surface area with overset grids have become available only recently.[46] In brief, the computational method locates the overlap regions of the neighboring grids in the overset grid framework and generates a composite (zipper) surface grid consisting of nonoverlapping quadrilaterals and triangles. The aerodynamic force and moment coefficients are determined using this accurate surface area information and aerodynamic loads. The drag increase due to the open cavity, so determined from CFD at WT and cruise flight conditions, respectively, is given in terms of equivalent flat plate area of 0.17 and 0.25 m^2. This drag increase is less than 2% of the aircraft drag.

Conclusions

A Navier–Stokes CFD investigation is undertaken to evaluate the Boeing 747-SP aircraft having a recessed D-shaped aperture cavity with barrel doors, a split aft ramp for shear-layer control, and a truss telescope as the SOFIA platform. Computational results of unsteady flow and cavity acoustics are presented for the WT and flight conditions and compared with experimental data. Important findings from these comparisons are 1) the time-averaged surface pressures on the empennage are in good agreement with experiments; 2) scaled flight CFD sound pressure levels are in general agreement with experiments, but the WT condition CFD results are overpredicted by 1–5 dB due to a smaller number of sampling data points; 3) an acoustic tone of 440 Hz predicted by CFD at WT condition (26 Hz for the full configuration in cruise flight) appears to be the dominant noise source for this cavity and is in agreement with experimental findings; and 4) the drag increase due to open cavity calculated by CFD is less than 2% of the aircraft drag.

References

[1]Rose, W., "SOFIA Wind Tunnel Data Analysis and Implications for Full-Scale Aircraft," Rose Engineering Research, Inc., TR, Incline Village, NV, Dec. 1990.

[2]Rose, W., "SOFIA—Aft Cavities Wind Tunnel Test—Pre-test Report," Rose Engineering Research, Inc., TR, Incline Village, NV, Feb. 1993.

[3]Rose, W., "SOFIA—Aft Cavities Wind Tunnel Test—Final Report," Rose Engineering Research, Inc., TR, Incline Village, NV, Dec. 1994.

[4]Atwood, C. A., "Navier–Stokes Simulations of Unsteady Transonic Flow Phenomena," NASA TM-103962, Aug. 1992.

[5]Atwood, C. A., and Van Dalsem, W. R., "Flowfield Simulation About the Statospheric Observatory for Infrared Astronomy," *Journal of Aircraft*, Vol. 30, No. 5, 1993, pp. 719–727.

[6]Atwood, C. A., "Unsteady Fluid and Optical Flow Simulation of Transonic Aero-Windows," AIAA Paper 93-3017, July 1993.

[7]Atwood, C. A., "Selected Computations of Transonic Cavity Flows," *Computational Aero- and Hydro-acoustics, ASME 1993 Fluids Engineering Conference*, FED-Vol. 147, American Society of Mechanical Engineers, New York, NY, 1993, pp. 7–18.

[8]Klotz, S. P., "The 747-SP SOFIA Platform: A Comparison of CFD Simulations and Wind Tunnel Experiments," TR 95-02, MCAT, Inc., San Jose, CA, April 1995.

[9]Srinivasan, G. R., "Flowfield and Acoustic Characteristics of Telescope Cavity in SOFIA Platform," *Proceedings of the AIAA 13th Applied Aerodynamics Conference*, AIAA, Washington, DC, 1995, pp. 801–823.

[10]Srinivasan, G. R., "Unsteady Flowfield and Cavity Acoustics of the Stratospheric Observatory for Infrared Astronomy," *Journal of Spacecraft and Rockets*, Vol. 34, No. 3, 1997, pp. 372–378.

[11]Machak, D., Srinivasan, G. R., and Klotz, S. P., "Aerodynamic Characteristics of the Stratospheric Observatory for Infrared Astronomy," AIAA Paper 95-0398, Jan. 1995.

[12]Srinivasan, G. R., and Klotz, S. P., "Features of Cavity Flow and Acoustics of the Stratospheric Observatory for Infrared Astronomy," *Proceedings of the ASME International Symposium on Advances in Domain Decomposition Methods for Fluid Flow Problems*, Paper FEDSM97-3647, American Society of Mechanical Engineers, New York, 1997, pp. 1–8.

[13]Komerath, N. M., Ahuja, K. K., and Chambers, F. W., "Prediction and Measurement of Flows over Cavities—A Survey," AIAA Paper 87-0166, Jan. 1987.

[14]Srinivasan, S., and Baysal, O., "Navier–Stokes Calculations of Transonic Flow Past Cavities," *Journal of Fluids Engineering*, Vol. 113, No. 3, 1991, pp. 368–376.

[15]Baysal, O., Yen, G.-W., and Fouladi, K., "Navier–Stokes Computations of Cavity Aeroacoustics with Suppression Devices," *Journal of Vibration and Acoustics*, Vol. 116, No. 1, 1994, pp. 105–112.

[16]Baysal, O., and Stallings, R. L., Jr., "Computational and Experimental Investigation of Cavity Flowfields," *AIAA Journal*, Vol. 26, No. 1, 1988, pp. 6, 7.

[17]Vakili, A. D., and Wolfe, R., "Active Control of Cavity Aeroacoustics in High-Speed Flows," AIAA Paper 95-0678, Jan. 1995.

[18]Rizetta, D., "Numerical Simulation of Supersonic Flow over a Three-Dimensional Cavity," *AIAA Journal*, Vol. 26, No. 7, 1988, pp. 799–807.

[19]Hankey, W. L., and Shang, J. S., "Analyses of Pressure Oscillations in an Open Cavity," *AIAA Journal*, Vol. 18, No. 8, 1980, pp. 892–898.

[20]Rossiter, J. E., "Wind-Tunnel Experiments on the Flow over Rectangular Cavities at Subsonic and Transonic Speeds," Reports and Memorandum 3438, Ministry of Aviation, Aeronautical Research Council, London, Oct. 1964.

[21]Heller, H. H., Holmes, D. G., and Covert, E. E., "Flow-Induced Pressure Oscillations in Shallow Cavities," *Journal of Sound and Vibration*, Vol. 18, No. 6, 1971, pp. 545–553.

[22]Tracy, M. B., and Plentovich, E. B., "Cavity Unsteady-Pressure Measurements at Subsonic and Transonic Speeds," NASA TP-3669, Dec. 1997.

[23]Orkwis, P. D., Sekar, B., Chakravarthy, S., and Peroomian, O., "Comparison of Three Navier–Stokes Equations Solvers for Supersonic Open Cavity Simulations," AIAA Paper 97-3163, July 1997.

[24]Tam, C.-J., and Orkwis, P. D., "Comparison of Baldwin–Lomax Turbulence Models for Two-Dimensional Open Cavity Computations," *AIAA Journal*, Vol. 34, No. 3, 1996, pp. 629–631.

[25]Tam, C.-J., Orkwis, P. D., and Disimile, P. J., "Algebraic Turbulence Model Simulations of Supersonic Open-Cavity Flow Physics," *AIAA Journal*, Vol. 34, No. 11, 1996, pp. 2255–2260.

[26]Orkwis, P. D., Tam, C.-J., and Disimile, P. J., "Observations on Using Experimental Data as Boundary Conditions for Computations," *AIAA Journal*, Vol. 33, No. 1, 1995, pp. 176–178.

[27]Sinha, N., Dash, S. M., and Chidambaram, N., "A Perspective on the Simulation of Cavity Aeroacoustics," AIAA Paper 98-0286, Jan. 1998.

[28]Slimon, S., Davis, D., and Wagner, C., "Far-Field Aeroacoustic Computation of Unsteady Cavity Flows," AIAA Paper 98-0285, Jan. 1998.

[29]Buell, D. A., "An Experimental Investigation of the Airflow over a Cavity with Antiresonance Devices," NASA TN-D-6205, March 1971.

[30]Buell, D. A., "Airloads Near the Open Port of a One-Meter Airborne Telescope," AIAA Paper 75-71, Jan. 1975.

[31]Buning, P. G., and Chan, W. M., "OVERFLOW User's Manual, Version 1.7u," NASA Ames Research Center, March 1997.

[32]Pulliam, T. H., and Chaussee, D. S., "A Diagonal Form of an Implicit Approximate-Factorization Algorithm," *Journal of Computational Physics*, Vol. 39, No. 2, 1981, pp. 347–363.

[33]Baldwin, B. S., and Lomax, H., "Thin-Layer Approximation and Algebraic Model for Separated Turbulent Flows," AIAA Paper 78-257, Jan. 1978.

[34]Steinbrenner, J. P., Chawner, J. R., and Fouts, C. L., "A Structured Approach to Interactive Multiple Block Grid Generation," *AGARD Fluid Dynamics Panel Specialists Meeting on Mesh Generation for Complex Three-Dimensional Configurations*, CP-464, AGARD, 1989, pp. 8.1–8.12.

[35]Chan, W. M., and Steger, J. L., "A Generalized Scheme for Three-Dimensional Hyperbolic Grid Generation," AIAA Paper 91-1588, June 1991.

[36]Klotz, S. P., "Computational Fluid Dynamic Grids in the D-Shaped Telescope Aperture Configuration of the SOFIA Aircraft Platform," Progress Rept. 13, MCAT, Inc., San Jose, CA, Jan. 1996.

[37]Benek, J. A., Buning, P. G., and Steger, J. L., "Three-Dimensional Chimera Grid Embedding Technique," AIAA Paper 85-1523, July 1985.

[38]Suhs, N. E., and Tramel, R. W., "PEGSUS 4.0 User's Manual," AEDC-TR-91-8, Arnold Engineering Development Center, Arnold AFB, TN, Nov. 1991.

[39]Srinivasan, G. R., "Influence of Cavity Aperture and Telescope Shape on Acoustics and Unsteady Flow of the SOFIA," AIAA Paper 98-0413, Jan. 1998.

[40]Srinivasan, G. R., "Computational Simulation of the SOFIA at Wind Tunnel and Cruise Flight Conditions," Final Rept., Sterling Software, Moffett Field, CA, March 1998.

[41]Kao, D. L., and Shen, H.-W., "Numerical Surface Flow Visualization," AIAA Paper 98-0076, Jan. 1998.

[42]Cabral, B., and Leedom, L., "Imaging Vector Fields Using Line Integral Convolution," *Proceedings of Special Interest Group on Computer Graphics '93*, Association of Computing Machinery, New York, 1993, pp. 263–272.

[43]Chaderjian, N., and Schiff, L., "Navier–Stokes Analysis of a Delta Wing in Static and Dynamic Roll," AIAA Paper 95-1868, June 1995.

[44]Press, W. H., Teukolsky, S. A., Vetterling, W. T., and Flannery, B. P., *Numerical Recipes in FORTRAN*, Cambridge Univ. Press, Cambridge, England, U.K., 1992, p. 167.

[45]Lane, D. A., "UFAT—A Particle Tracer for Time-Dependent Flow Fields," *Proceedings of the Institute of Electrical and Electronics Engineers Visualization '94*, IEEE Publications, Piscataway, NJ, 1994, pp. 257–264.

[46]Chan, W. M., and Buning, P., "Zipper Grids for Force and Moment Computation on Overset Grids," AIAA Paper 95-1681, June 1995.